Influence of Bi substitution with rare-earth elements on the transport properties of BiCuSeO oxyselenides

Andrei Novitskii,[a,b,*] Illia Serhiienko,[a] Sergey Novikov,[b] Yerzhan Ashim,[c] Mark Zheleznyi,[a,d] Kirill Kuskov,[a] Daria Pankratova,[a,‡] Petr Konstantinov,[b] Andrei Voronin,[a] Oleg A. Tretiakov,[c] Talgat Inerbaev,[e,f] Alexander Burkov,[b] Vladimir Khovaylo[a]

[a] National University of Science and Technology MISIS, 119049 Moscow, Russia

[b] Ioffe Institute, 194021 St. Petersburg, Russia

[c] The University of New South Wales, 2052 Sydney, Australia

[d] A.A. Baikov Institute of Metallurgy and Materials Science, Russian Academy of Sciences, 119334 Moscow, Russia

[e] Sobolev Institute of Geology and Mineralogy, 630090 Novosibirsk, Russia

[f] L.N. Gumilyov Eurasian National University, 010000 Nur-Sultan, Kazakhstan

[‡] Present address: Luleå University of Technology, 97187 Luleå, Sweden

[*] E-mail: novitskiy@misis.ru

Experimental details

Ball-milling was carried out using a Pulverisette 7 planetary micro mill (Fritsch, Germany) with zirconium oxide balls (diameter of 5 mm, powder-to-ball ratio of 1:5) and vials (45 ml) in an argon atmosphere in reverse mode. To avoid overheating of the powders, the milling periods never exceeded 5 minutes. For instance, ball milling for 8 hours was performed as 96 cycles of "5 min milling + 5 min break". In order to obtain bulk samples, the ball-milled powders were put into cylindrical graphite die with a diameter of 12.7 mm and compressed in an SPS machine at room temperature for 1 minute under a uniaxial pressure of 50 MPa in an evacuated to ~10 Pa chamber, which then was filled with Ar. The temperature of the samples was gradually raised to a sintering temperature of 973 K with a heating rate of 50 K min^{-1}; after the dwelling for 5 min at a sintering temperature, the pressure was gradually reduced to ~10 MPa, and the sample was cooled to room temperature with a cooling rate of 20 K min^{-1}. Figure S1 displays a schematic illustration of the synthesis route used in this work. For comparative analysis, one pristine BiCuSeO sample was prepared without using the ball milling (without BM-1, BM-2, and BM-3 steps, respectively; see Fig. S1) with hand-grinding instead. All the densified disk-shaped specimens had a dimension of 12.7 mm diameter × 10 mm height, respectively. Obtained bulks were annealed at 973 K for 6 hours in an argon atmosphere.

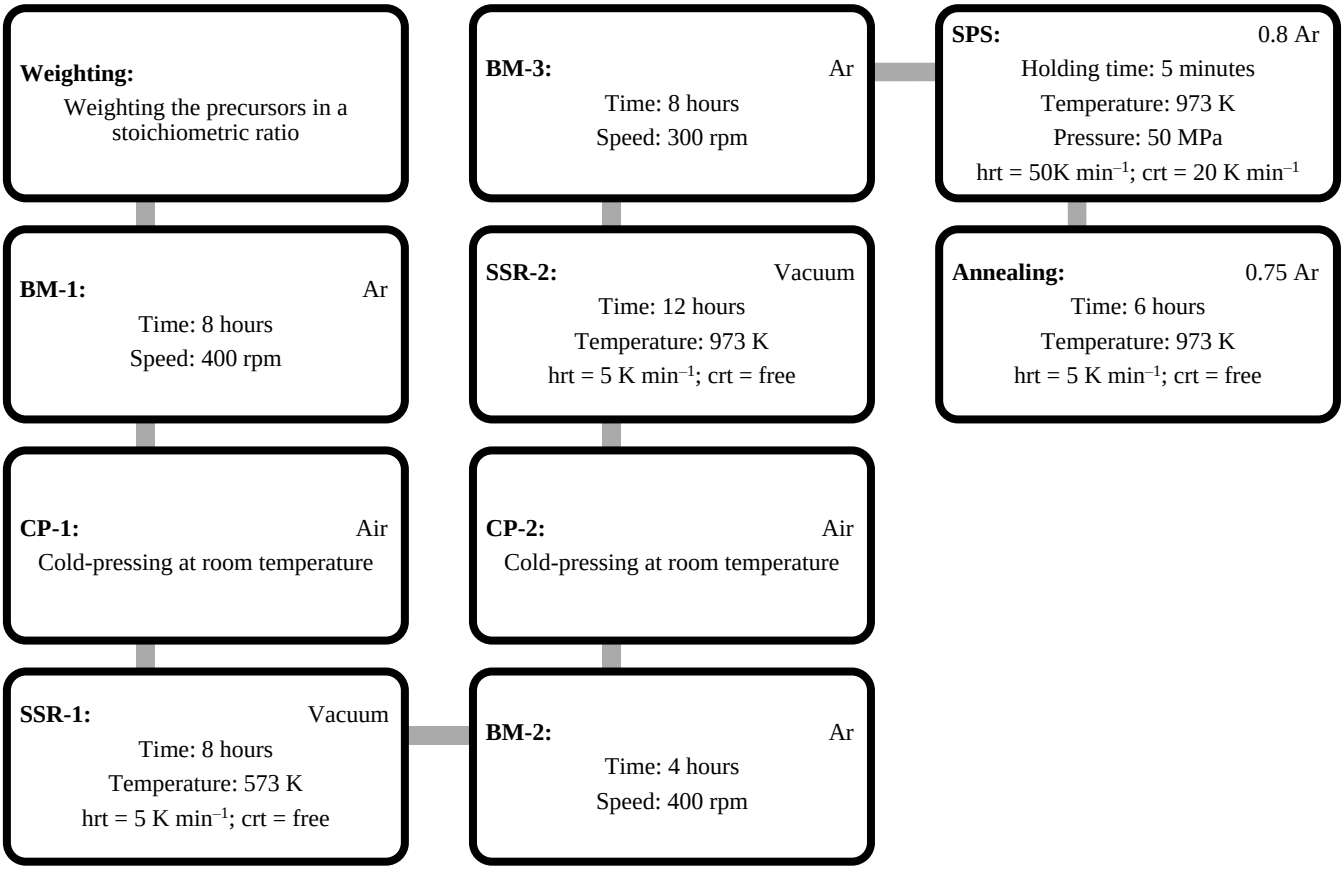

Figure S1. Schematic illustration of the fabrication route for the $Bi_{1-x}R_xCuSeO$ (R = La or Pr, x = 0, 0.02, 0.04, 0.06, 0.08) samples (hrt and crt are heating and cooling rates, respectively).

Thermal diffusivity and heat capacity

The thermal diffusivity (χ) was measured by a laser flash method (LFA 457 MicroFlash, Netzsch, Germany) under a continuous Ar flow, and the data is shown in Fig. S2a. Generally, experimental data for the specific heat capacity of BiCuSeO oxyselenides can be fitted and analyzed by the Debye model as it was shown by many reports (see Fig. S2b).[1,2] In this work, the heat capacity was calculated by the Debye model (similar to the Dulong-Petit law when $T > \theta_D$):[3,4]

$$C_p = \gamma T + \frac{9Rn}{M} \cdot \left(\frac{T}{\theta_D}\right)^3 \cdot \int_0^{\theta_D/T} \frac{x^4 e^x}{\left(e^x - 1\right)^2} dx, \quad \text{(S1)}$$

where γ is the Sommerfeld coefficient, R is the ideal gas constant, n is the number of atoms, M is the molar mass of a primitive cell, θ_D is the Debye temperature, and $x = h\nu/k_B T$. The Debye temperature and the Sommerfeld coefficient were assumed to be independent of chemical composition; θ_D = 243 K and $\gamma = 3.075 \cdot 10^{-7}$ J g^{-1} K^{-2} as reported by C. Barreteau and L. Pan.[2,5] The first term of Equation (S1) corresponds to the electronic part, while the second one corresponds to the phonon contribution to the C_p. For undoped BiCuSeO the C_p approaches the Dulong-Petit limit at high temperature ($C_p = 3nR/M$; 0.271 J·g^{-1}·K^{-1} for BiCuSeO). However, it can be expected that due to a significant difference in atomic mass between La, Pr, and Bi (138.91, 140.91, and 208.98, respectively) the heat capacity of the *R*-doped samples should be slightly higher than for the undoped sample. All calculations were carried out considering this mass difference (see Fig. S2c).

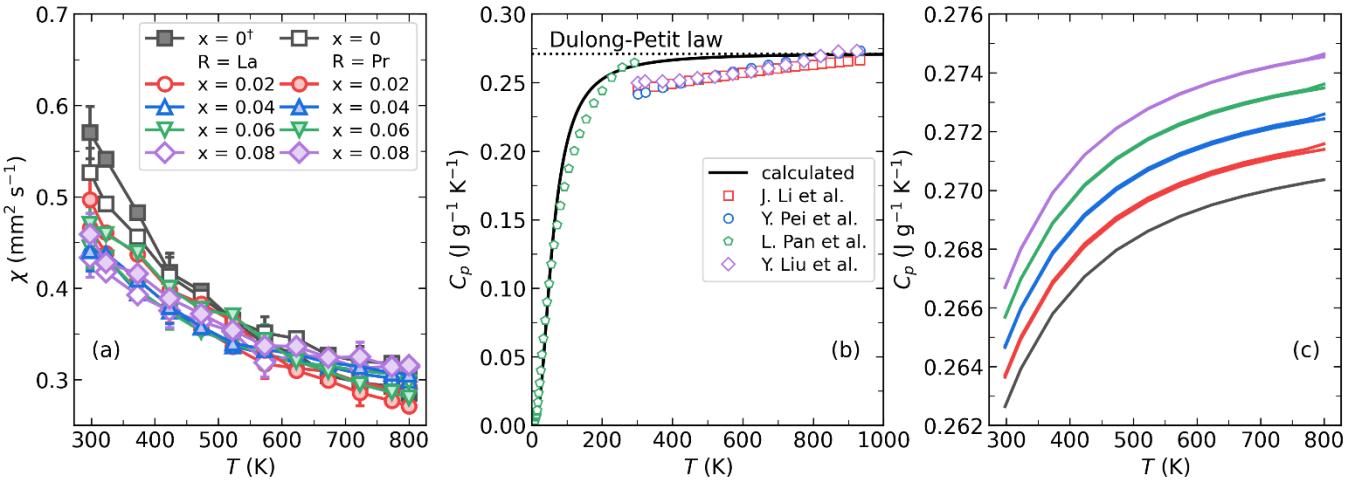

Figure S2. Temperature dependence of (a) the thermal diffusivity, χ, for $Bi_{1-x}R_xCuSeO$ (R = La or Pr, x = 0 – 0.08), (b) the specific hear capacity calculated by Debye model (black solid line) and experimental data from previous reports[5–8] (adapted from Ref.[9]) and (c) the calculated heat capacity (solid lines) for doped $Bi_{1-x}R_xCuSeO$ (R = La or Pr, x = 0 – 0.08) used for thermal conductivity calculation.

Rietveld refinement

The final refinement was carried out assuming a tetragonal symmetry with a space group of *P4/nmm* and taking the pseudo-Voigt function for the peak profiles. Figure S3 displays the observed (circles) and fitted (solid red lines) diffraction patterns taken at room temperature, with their differences plotted below the XRD patterns (solid blue lines). They agree very well with $R_p \leq 8.6\%$, $R_{wp} \leq 10.9\%$, and $\chi^2 \leq 2.3$.

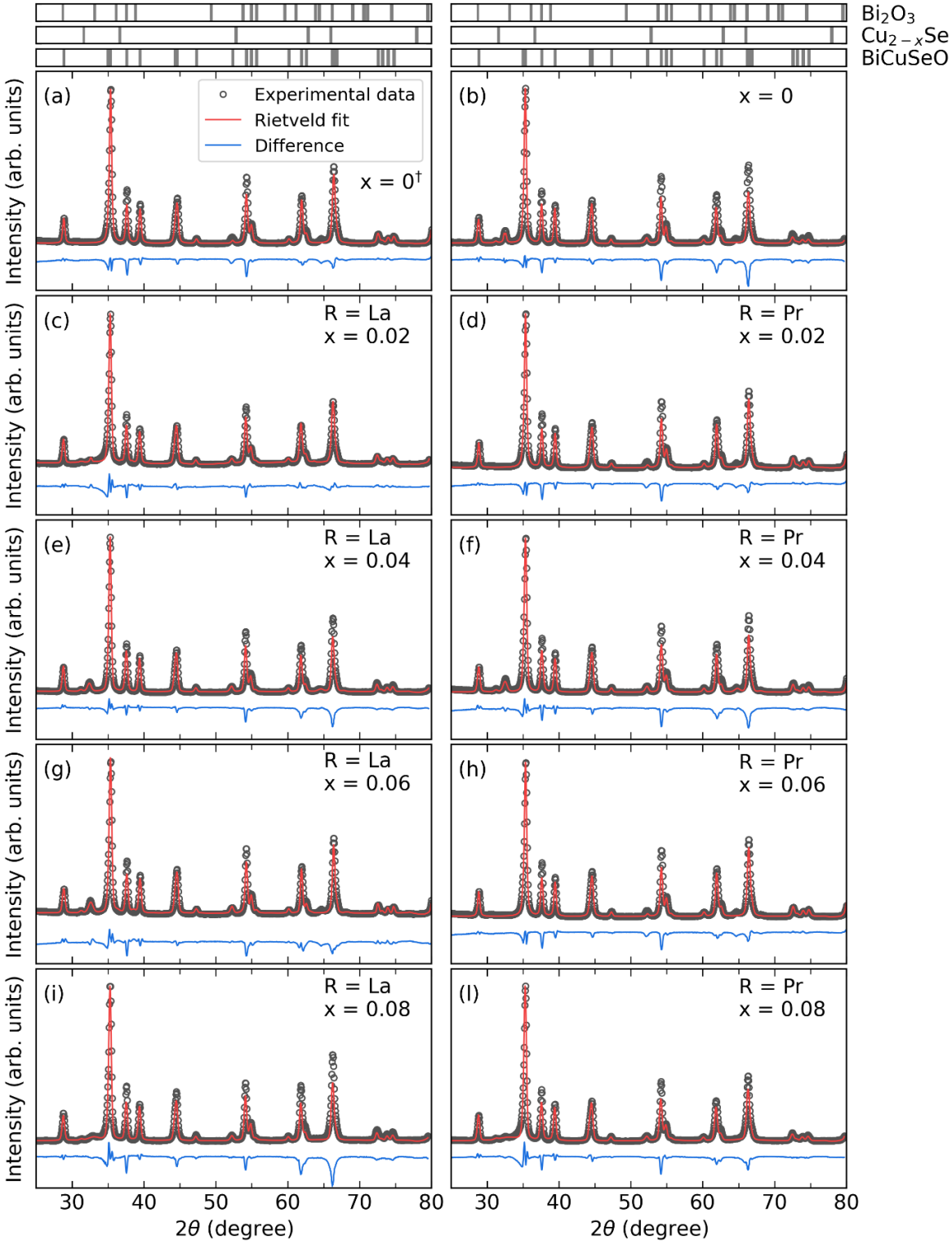

Figure S3. Rietveld refinement of powder XRD pattern for BiCuSeO† and $Bi_{1-x}R_xCuSeO$ (R = La or Pr, x = 0 – 0.08) specimens.

Compositional and structural analyses

Energy-dispersive X-ray spectroscopy.

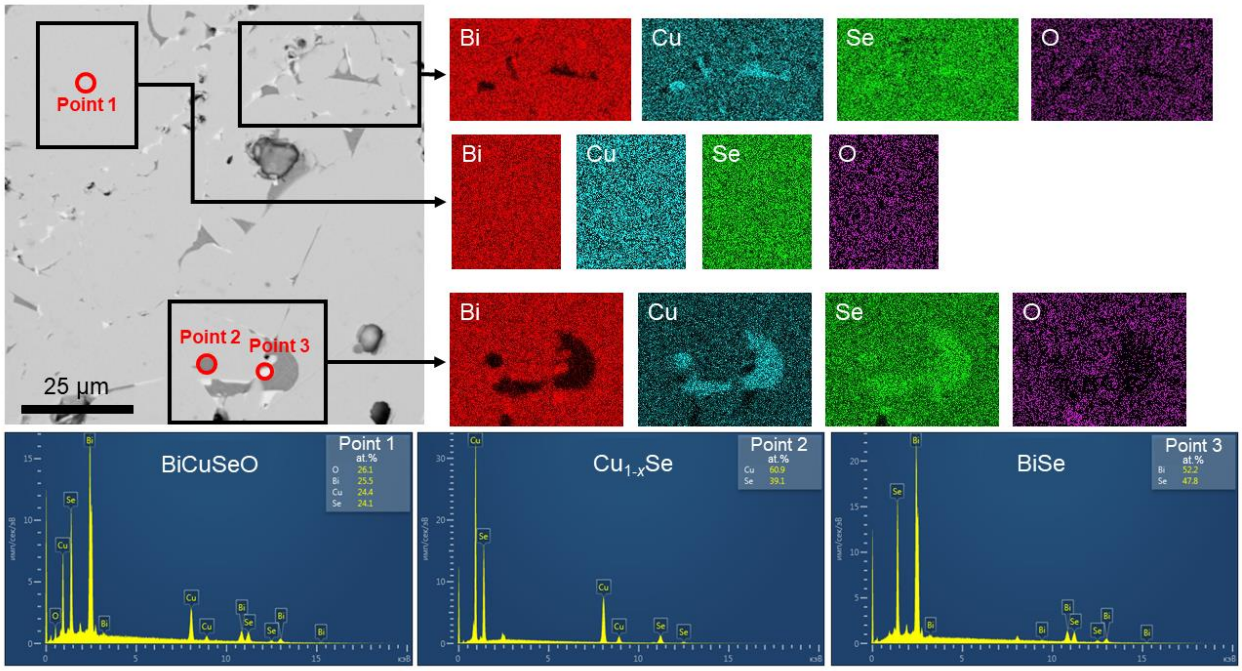

Figure S4. SEM image of the polished surface, EDS spectra, and mapping for pristine BiCuSeO bulk prepared from non-milled powder (hereinafter labeled as BiCuSeO†).

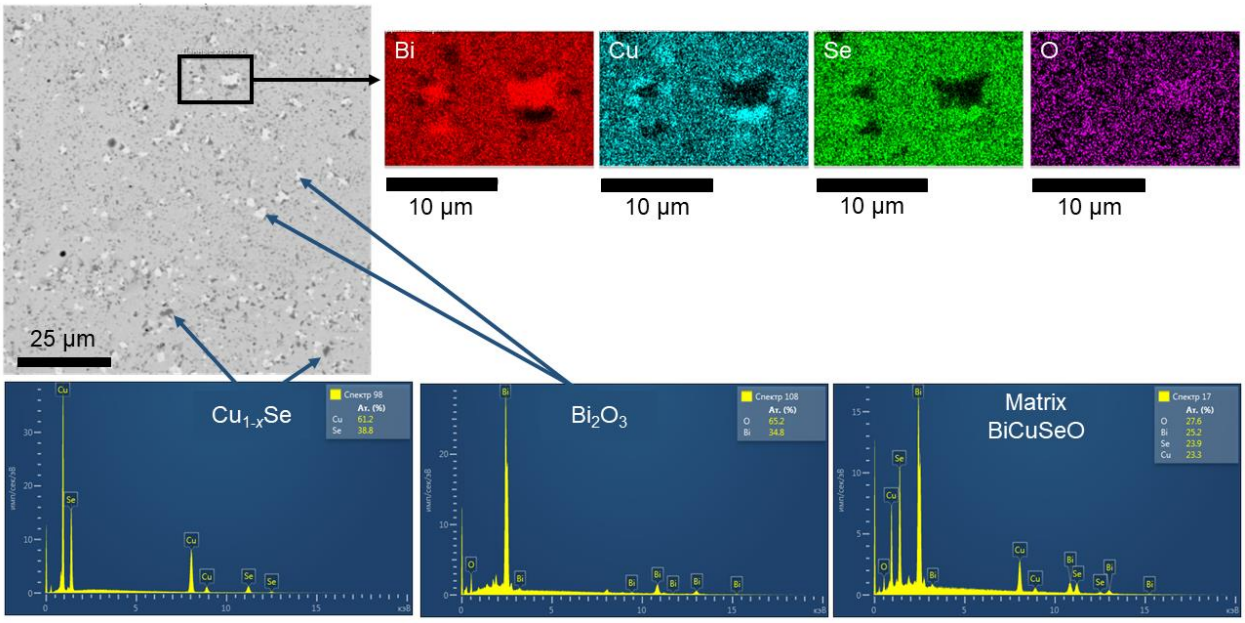

Figure S5. SEM image of the polished surface, EDS spectra, and mapping for pristine BiCuSeO bulk prepared from ball milled powder.

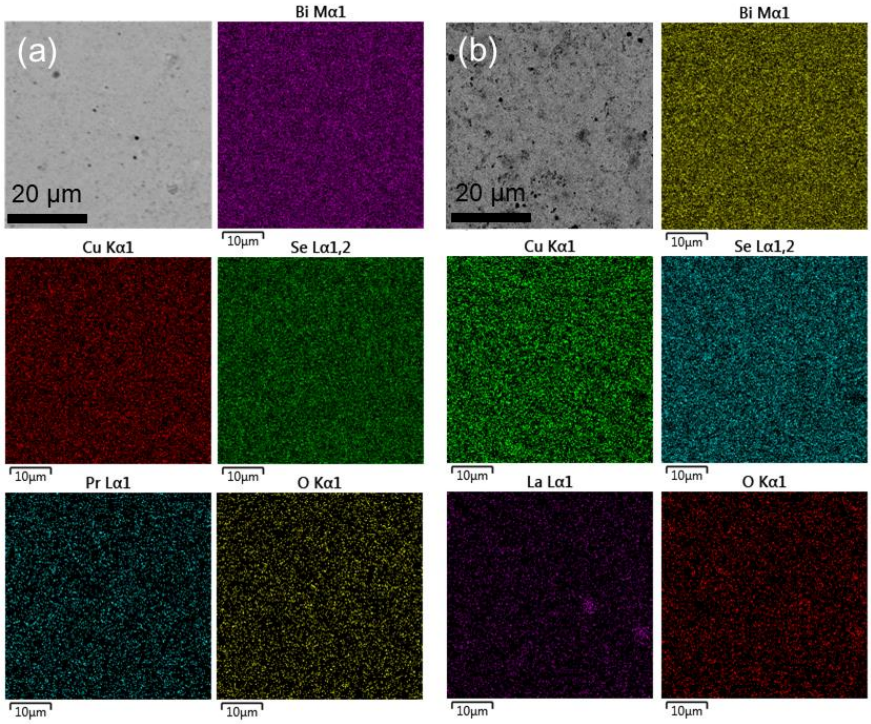

Figure S6. SEM micrographs of the polished surfaces and corresponding EDS mapping for (a) $Bi_{0.96}Pr_{0.04}CuSeO$ and (b) $Bi_{0.96}La_{0.04}CuSeO$.

X-ray diffraction and X-ray fluorescence. XRD pattern evolution for the starting mixture with a nominal composition of BiCuSeO during the solid-state fabrication route followed by SPS is shown in Figure S7a. The elemental composition of the studied $Bi_{1-x}R_xCuSeO$ (R = La or Pr, $0 \le x \le 0.08$) samples were examined by X-ray fluorescence (XRF), the XRF spectra were taken with a ZSK Primus 9 II spectrometer (Rigaku, Japan), employing the standard setup at room temperature. The XRF spectra for some samples are shown in Figure S7b. The relative elemental proportion of (Bi + R):Cu:Se:O determined from XRF and EDS can be found in the main text (see Table 2).

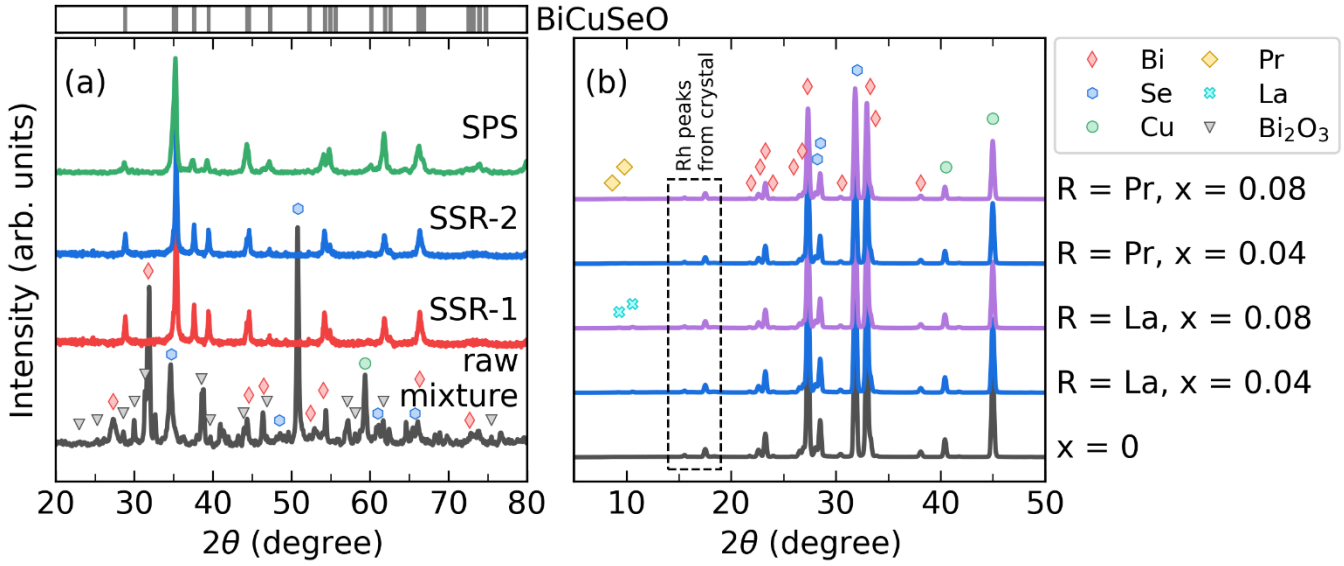

Figure S7. (a) XRD patterns for raw mixture, powders after first (SSR-1) and second (SSR-2) steps of solid-state reaction, after spark plasma sintering for BiCuSeO; (b) XRF spectra for the $Bi_{1-x}R_xCuSeO$ (R = La or Pr, x = 0, 0.04, 0.08) samples.

Scanning electron microscopy. SEM images of the fractured cross-section of the densified BiCuSeO†, BiCuSeO, $Bi_{0.96}Pr_{0.04}CuSeO$, and $Bi_{0.96}La_{0.04}CuSeO$ samples are displayed in Figure S5. All the samples exhibited a similar lath-like microstructure with randomly arranged platelet grains stacked densely, which is typical for BiCuSeO based compounds. The grain size after SPS remained 5 – 20 μm for BiCuSeO† and 200 – 700 nm for $Bi_{1-x}R_xCuSeO$ (R = La or Pr, x = 0, 0.04, 0.08).

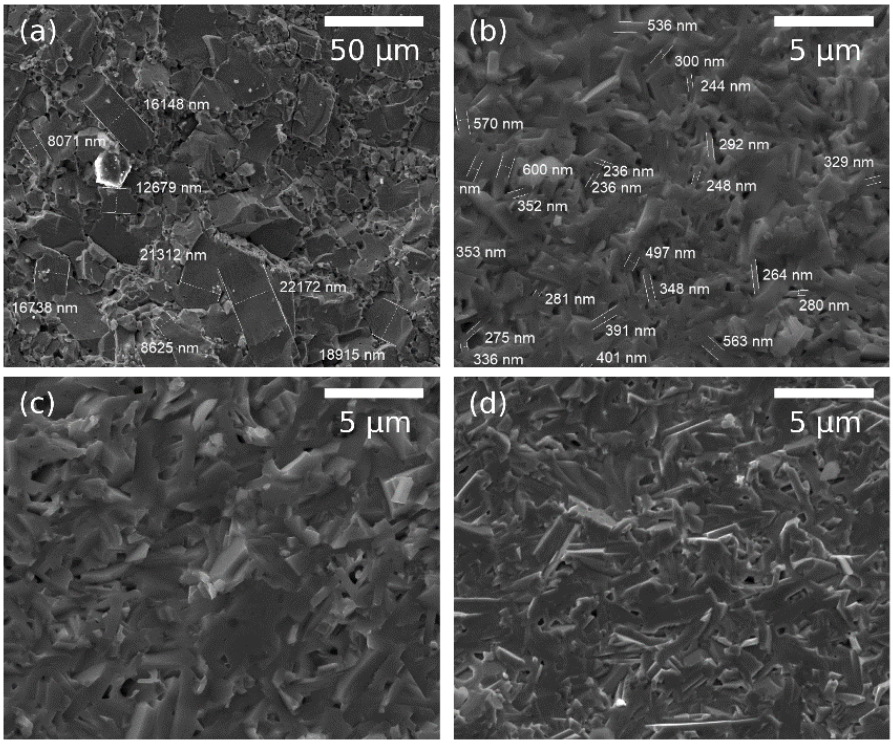

Figure S8. SEM micrographs of the fracture surfaces for (a) BiCuSeO†, (b) BiCuSeO, (c) $Bi_{0.96}Pr_{0.04}CuSeO$, and (d) $Bi_{0.96}La_{0.04}CuSeO$ bulk sample.

First principles calculations

The total and partial DOS. The computed projected density-of-states for $Bi_{59}La_5Cu_{64}Se_{64}O_{64}$ are in good agreement with the results for LaCuSeO reported by H. Hiramatsu *et al.*[10]

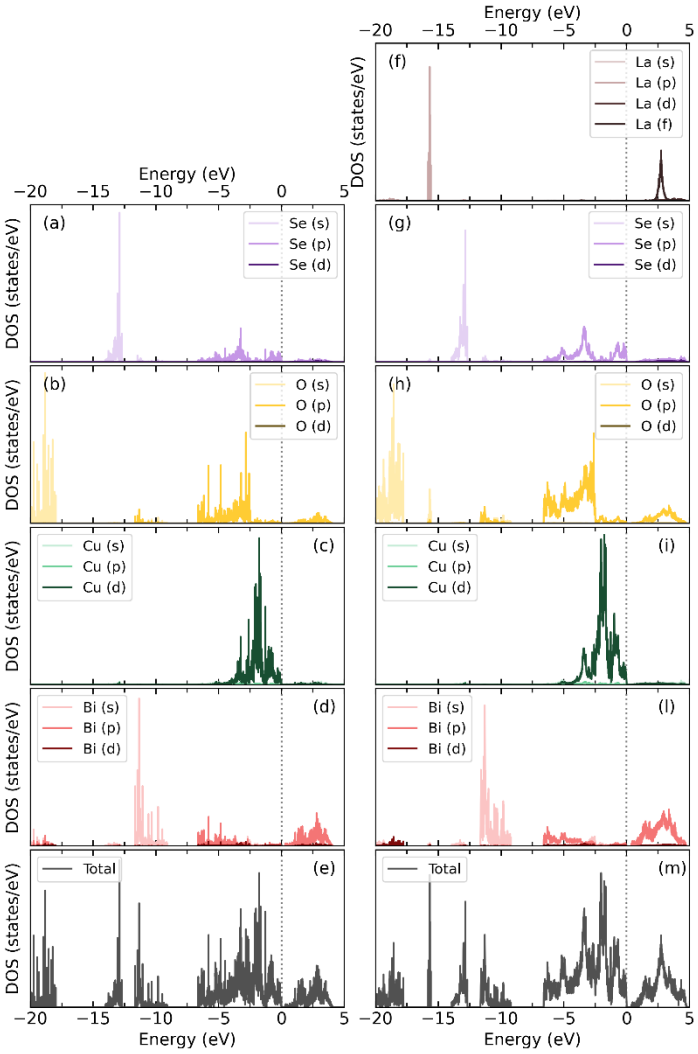

Figure S9. The total DOS and partial DOSs of (a) $Bi_{64}Cu_{64}Se_{64}O_{64}$ and (b) $Bi_{59}La_5Cu_{64}Se_{64}O_{64}$.

Projected band structures. Projected band structures, where the contributions of Bi *p*, Cu *d*, Se *p* to a band are plotted.[11]

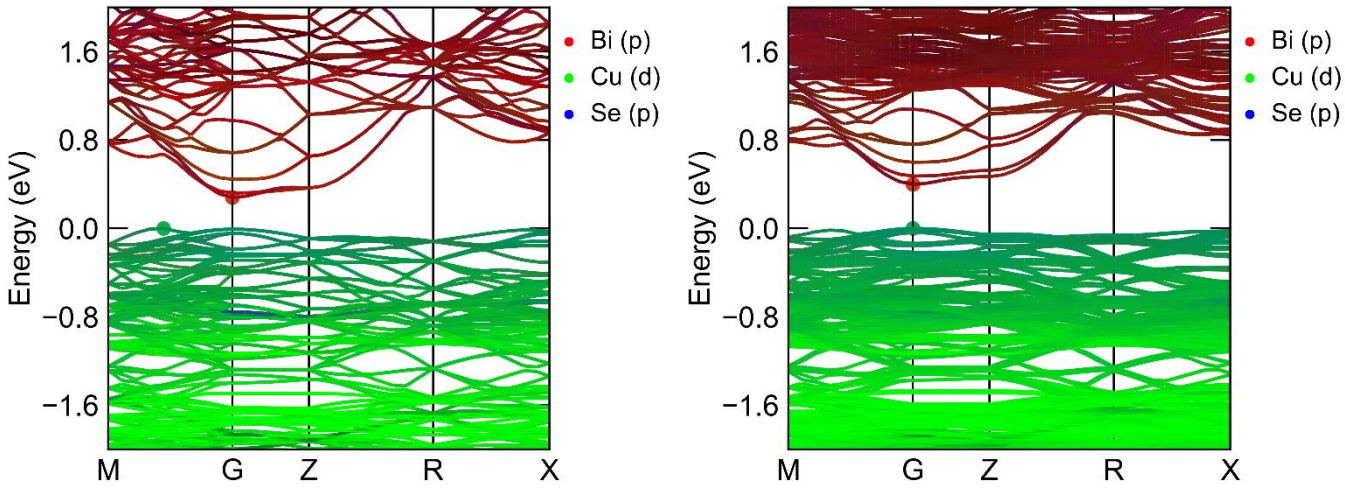

Figure S10. Projected band structure of (left) $Bi_{64}Cu_{64}Se_{64}O_{64}$ and (right) $Bi_{59}La_5Cu_{64}Se_{64}O_{64}$.

Electrical and thermal transport properties

Pristine BiCuSeO. Transport data (σ, α, κ_{lat}, zT) for pristine BiCuSeO† and BiCuSeO are presented in Fig. S11, some data from literature is also displayed.[12–14] Results for BiCuSeO† are in good consistent with previous reports: the temperature dependence of the electrical conductivity exhibits a non-degenerate behaviour; moreover, the temperature dependence of the Seebeck coefficient is also in good agreement and shows low values at T < 600 K as was also reported by F. Li *et al*. for BiCuSeO fabricated without ball milling during powder preparation; noteworthy values of the lattice thermal conductivity measured in parallel to SPS applied pressure direction are also close to those presented by F. Li *et al*. for both ball-milled (BM) and non-ball-milled (NBM) specimens. On the other hand, values determined in the perpendicular direction are higher by ~20%, which can be attributed to the preferential grain growth in the perpendicular direction to the axis applied during SPS uniaxial pressure as shown in Figs. S12a – d.

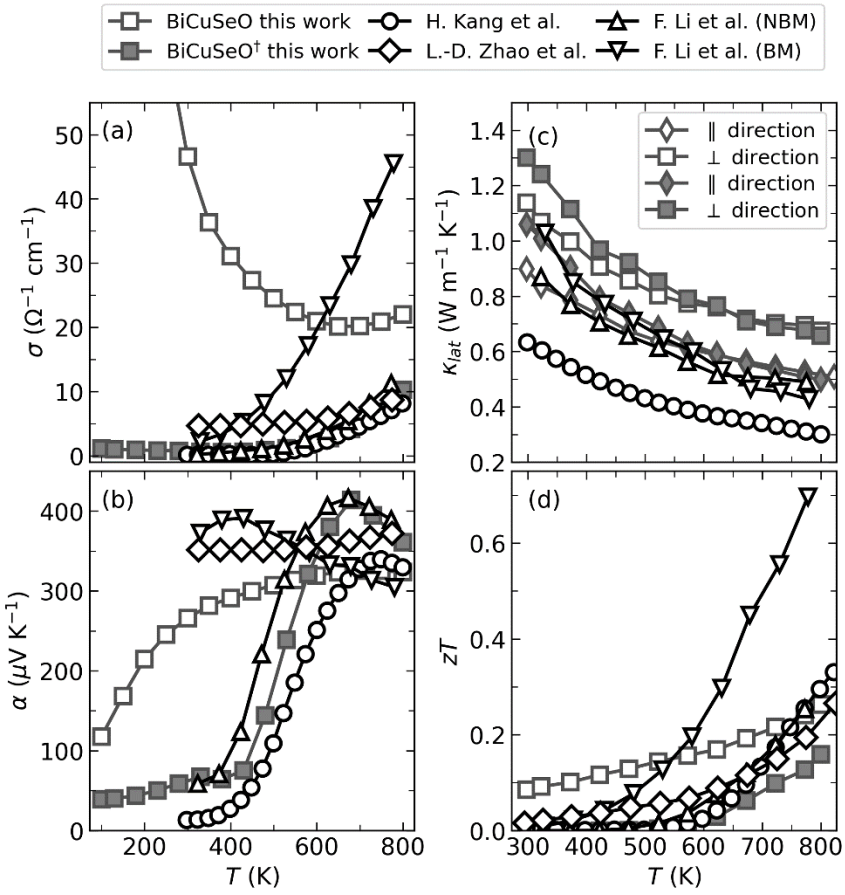

Figure S11. Temperature dependence of (a) the electrical conductivity, (b) the Seebeck coefficient, (c) the lattice thermal conductivity and (d) the figure of merit zT for BiCuSeO†, and BiCuSeO samples. Data from previous reports are also given for comparison.[12–14]

Anisotropy. In order to perform all the measurements with consideration of the possible anisotropy, the samples were cut in two pieces getting cylinder-shaped and parallelepiped-shaped specimens (see Fig. S12). These two slices were used for the thermal diffusivity measurements in the parallel and the perpendicular to the SPS pressure direction, respectively (see Fig. S12e). Then the slices were cut one more time to get bars for the electrical transport properties measurements in both directions (Fig. S12e). The electrical transport properties were measured at Ioffe Institute (Saint-Petersburg, Russia) using a homemade system[15] and for some samples repeated measurements were carried out at the National University of Science and

Technology MISIS (Moscow, Russia) using a laboratory-made system developed by Ltd. Cryotel (Moscow, Russia). All the measured data were in excellent agreement (see Figs. S11a and S11b).

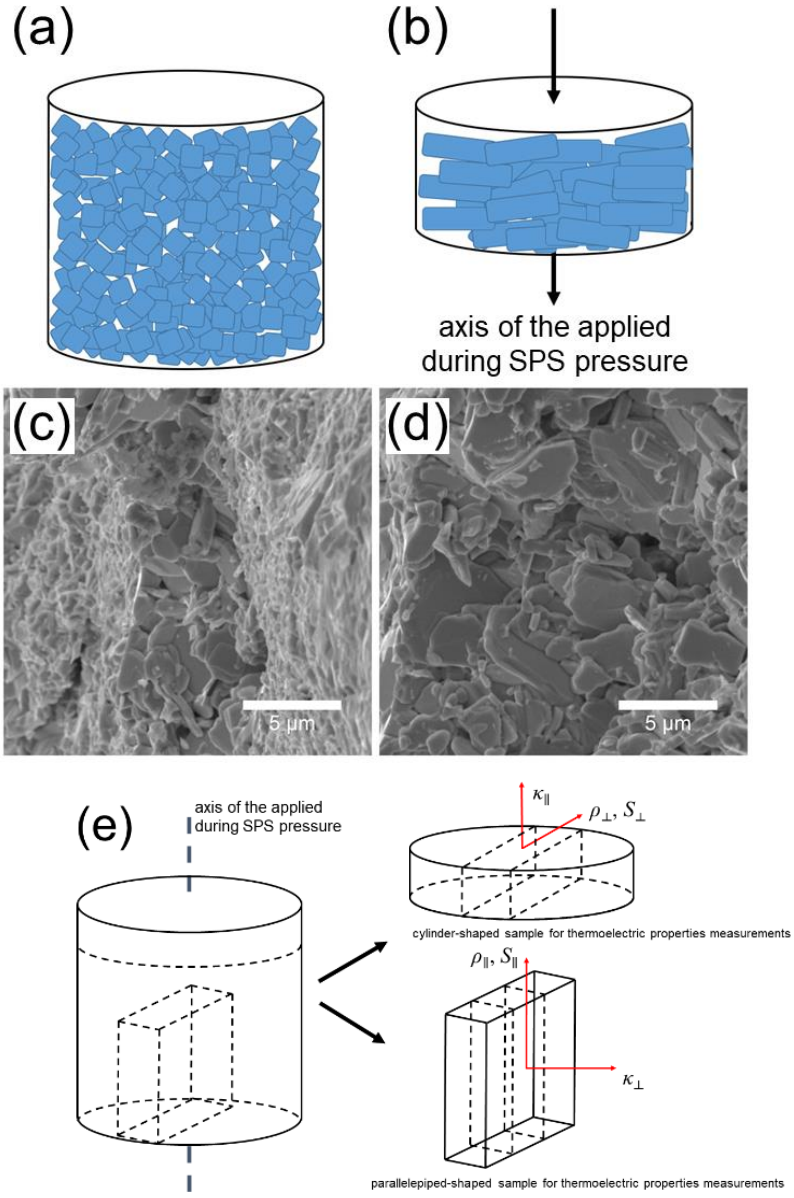

Figure S12. Schematic illustration of the (a) BiCuSeO powder particles before SPS and (b) the lamellar grains of the bulk BiCuSeO after SPS. SEM images of the fractured surfaces for (c) BiCuSeO and (d) $Bi_{0.96}La_{0.04}CuSeO$ bulks. (e) Schematic illustration of the measured direction for electrical and thermal transport properties.

The ratios of the electrical resistivity and the Seebeck coefficient measured in parallel and perpendicular directions do not outperform 5%, so the electrical transport properties for BiCuSeO polycrystalline specimens understudy can be assumed to be isotropic (Fig. S13). However, the thermal conductivity values indicated a difference of ~20% for those measured in the parallel and the perpendicular directions, respectively. It can be suggested that the observed anisotropy in the thermal conductivity is mainly attributed to a preferential grain growth along the perpendicular to the applied pressure direction during the SPS process (see Figs. S11c, S12a, S12b, S13e, and S13f), which is in a good consistent with the literature data and confirmed by SEM studies (see Figs. S12c, S12d).[16–18] For doped samples, the difference is decreased to 10 – 15% due to the increased electronic contribution to the total thermal conductivity.

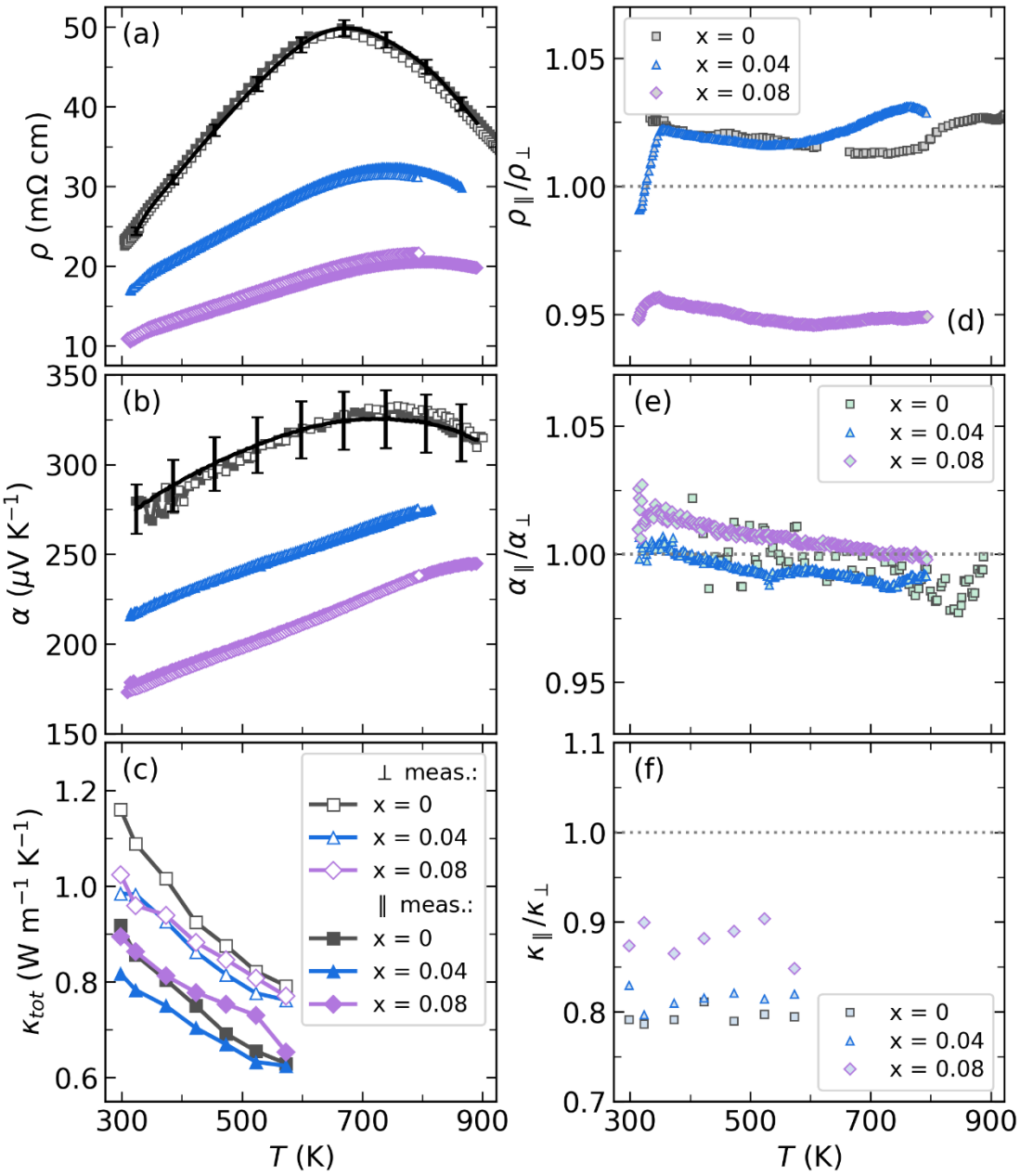

Figure S13. Electrical and thermal transport properties for $Bi_{1-x}Pr_xCuSeO$ (x = 0, 0.04, 0.08) measured in the parallel (∥) and the perpendicular (⊥) to SPS applied pressure direction. Temperature dependence of (a) the electrical resistivity, (b) the Seebeck coefficient, and (c) the total thermal conductivity. The ratios of the corresponding properties measured in different directions (d) $\rho_{\parallel}/\rho_{\perp}$ (e) $\alpha_{\parallel}/\alpha_{\perp}$, and (f) $\kappa_{\parallel}/\kappa_{\perp}$. (a, b) For α and ρ of pristine BiCuSeO sample black solid line represents values obtained from homemade equipment at Ioffe Institute (in ∥ direction), while filled and empty squares display results obtained from homemade equipment at NUST MISIS.

Single parabolic band model calculations

Despite the complex nonparabolic multiband electronic structure in BiCuSeO, the experimental transport data can be roughly analyzed using a single parabolic band model with relaxation time approximation. The equations shown below are valid for a single scattering mechanism where the energy dependence of the carrier relaxation time can be expressed by a simple power-law $\tau = \tau_0 E^{\lambda}$ (λ is the scattering parameter).[19] The Hall carrier concentration is related to the so-called chemical carrier concentration p *via* $p = p_H r_H$, where r_H is the Hall factor, which is given by

$$r_H = \frac{3}{2} F_{1/2}(\eta) \frac{(3/2 + 2\lambda) F_{2\lambda+1/2}(\eta)}{(3/2 + \lambda)^2 F_{\lambda+1/2}^2(\eta)}, \tag{S2}$$

with the j-th order Fermi integrals, $F_j(\eta)$ defined by

$$F_j(\eta) = \int_0^{\infty} \frac{\varepsilon^j}{1 + e^{\varepsilon - \eta}} d\varepsilon, \tag{S3}$$

where ε is the reduced carrier energy, η is the reduced electrochemical potential related to Fermi energy *via*

$$\eta = \frac{E_v - E_F}{k_B T}. \tag{S4}$$

Here $(E_v - E_F)$ is the Fermi energy with respect to the top of the valence band, k_B is the Boltzmann constant, λ is the scattering parameter related to the energy dependence of the carrier relaxation time, τ. η values could be obtained from analysis of the Seebeck coefficient experimental data (details below).[20] For complete degeneracy ($\eta > 5$) $r_H = 1$ regardless of the scattering mechanism and $\lambda = 0$ regardless of the η value (energy-independent charge carrier relaxation time); for nondegenerate semiconductors ($\eta < -1$), r_H tends to 1.93 for ionized impurities scattering ($\lambda = 3/2$), $r_H \rightarrow 1.11$ for polar optical phonon scattering ($\lambda = 1/2$), $r_H \rightarrow 1$ for charge-neutral impurity scattering ($\lambda = 0$) and $r_H \rightarrow 1.18$ for a scattering of carries with acoustic phonons ($\lambda = -1/2$).[19–22] The values of η and r_H showed in Table S1 were calculated assuming $\lambda = -1/2$ for acoustic phonon scattering as the main charge carrier scattering mechanism. It can be clearly seen that the *R*-doping leads to a degeneration of BiCuSeO, which is in good agreement with the experimental data (see Fig. 7).

Table S1. Room-temperature values of the Seebeck coefficient of $Bi_{1-x}R_xCuSeO$ (*R* = La or Pr, $x = 0 - 0.08$) samples; η, r_H, and m^* were calculated within a single parabolic band model with acoustic phonon scattering (SPB-APS)

Nominal composition	α (μV K^{-1})	η	r_H
BiCuSeO[†]	62	4.46	1.03
BiCuSeO	266	–0.91	1.16
$Bi_{0.98}La_{0.02}CuSeO$	243	–0.58	1.15
$Bi_{0.96}La_{0.04}CuSeO$	213	–0.13	1.14
$Bi_{0.94}La_{0.06}CuSeO$	186	0.32	1.13
$Bi_{0.94}La_{0.08}CuSeO$	173	0.56	1.12
$Bi_{0.98}Pr_{0.02}CuSeO$	232	–0.42	1.15
$Bi_{0.96}Pr_{0.04}CuSeO$	212	–0.12	1.14
$Bi_{0.94}Pr_{0.06}CuSeO$	173	0.56	1.12
$Bi_{0.92}Pr_{0.08}CuSeO$	169	0.63	1.12

Reduced chemical potential can be calculated from:

$$\alpha = \frac{k_B}{e}\left[\frac{(\lambda+5/2)F_{\lambda+3/2}(\eta)}{(\lambda+3/2)F_{\lambda+1/2}(\eta)} - \eta\right], \tag{S5}$$

where e is the electron charge.

Lorenz number can be calculated as follows:[19,20]

$$L(\eta) = \left(\frac{k_B}{e}\right)^2 \left(\frac{(\lambda+7/2)F_{\lambda+5/2}(\eta)}{(\lambda+3/2)F_{\lambda+1/2}(\eta)} - \left[\frac{(\lambda+5/2)F_{\lambda+3/2}(\eta)}{(\lambda+3/2)F_{\lambda+1/2}(\eta)}\right]^2\right). \tag{S6}$$

The calculated Lorenz number of all the samples decreases with temperature, while the Hall factor exhibits similar to the Seebeck coefficient temperature dependence, as shown in Figure S14. The Hall mobility can be modeled using

$$\mu_H = \frac{e\pi\hbar^4 C_{ll}}{\sqrt{2}(k_B T)^{3/2}(m_d^*)^{5/2}\Delta_{def}^2} \frac{(3/2+2\lambda)F_{2\lambda+1/2}(\eta)}{(3/2+\lambda)F_{\lambda+1/2}(\eta)}, \tag{S7}$$

where $\hbar$ is the reduced Planck's constant, C_{ll} is the elastic constant for longitudinal vibrations ($C_{ll} = dv_l^2$, where v_l is the longitudinal component of sound velocity), m_d^* is the density-of-states effective mass, and Δ_{def} is the deformation potential characterizing the carrier-phonon interaction (see Fig. S14c).

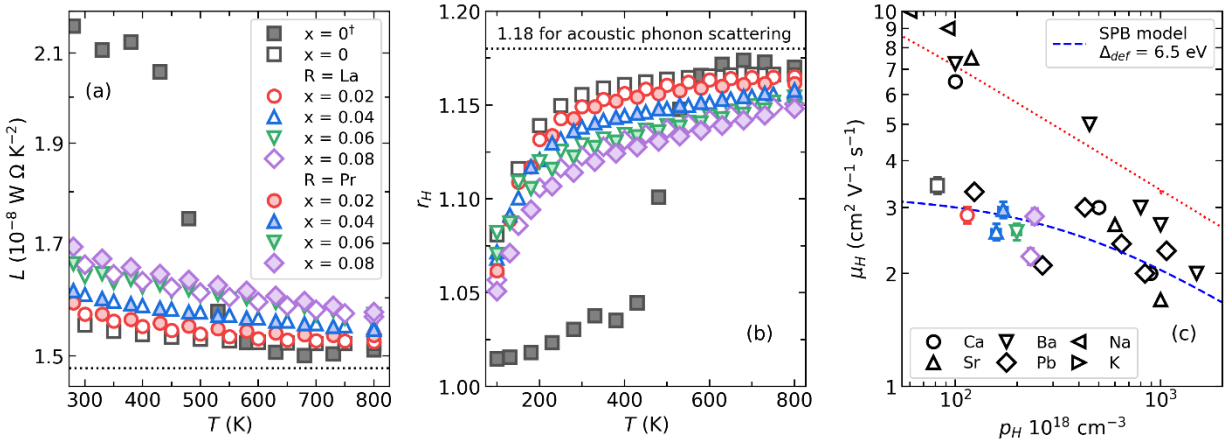

Figure S14. Temperature dependence of (a) the Lorenz number and (b) the Hall factor for $Bi_{1-x}R_xCuSeO$ (R = La or Pr, x = 0 – 0.08). (c) The Hall mobility versus the Hall carrier concentration for the samples at 300 K. The experimental data (colored symbols) are compared to theoretical curves calculated under the SPB model assuming carrier mobility is limited by acoustic phonon scattering (blue dashed curve), and data from previous reports are also given for comparison.[2,5,8,23–25]

Comparison with previous reports. Transport properties of the $Bi_{0.96}La_{0.04}CuSeO$ and $Bi_{0.96}Pr_{0.04}CuSeO$ (not optimally doped but with close chemical composition to other reported samples) were compared with those reported for other rare-earth doped BiCuSeO.[7,12,26–30] Difference in the temperature dependence of the electrical conductivity may originate from the fabrication technique and the initial number of defects in the system. Nevertheless, in general, all the thermoelectric properties for studied samples are in good agreement with those reported for other R-doped BiCuSeO (even for doping with the variable-valence elements such as Yb or Sm). This is also true for the figure of merit zT considering the uncertainty of its determination and possible overestimation for the cases when anisotropy of properties is not considered. Only Er- and Sm-doped samples exhibited zT > 0.4 at 800 K.

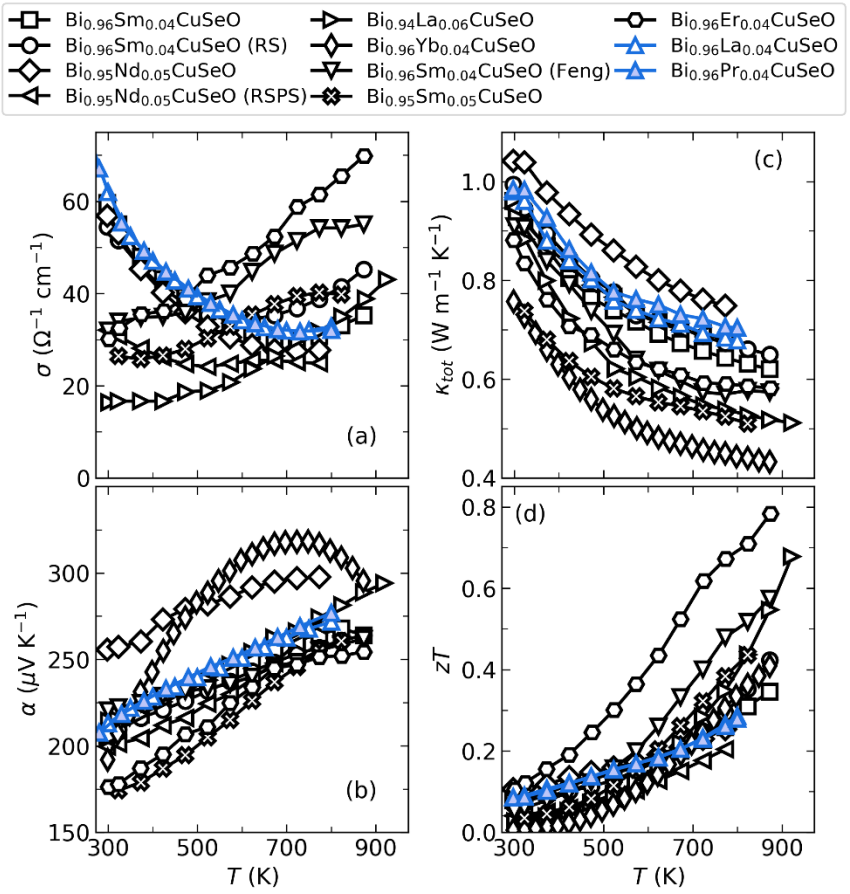

Figure S15. Temperature dependence of (a) the electrical conductivity, (b) the Seebeck coefficient, (c) the total thermal conductivity, and (d) the figure of merit ***z**T* for $Bi_{0.96}La_{0.04}CuSeO$ and $Bi_{0.96}Pr_{0.04}CuSeO$ samples, and data from previous reports.[7,12,26–30]

Thermal properties. For the theoretical calculations of the lattice thermal conductivity a modified Callaway's model was used: the normal scattering process was ignored and the Umklapp scattering term is altered from $BT^3\omega^2 e^{-\theta_D/T}$ to $BT\omega^2 e^{-\theta_D/3T}$ as was suggested by Slack for materials with the temperature dependence of $\kappa_{lat} \sim T^{-1}$ at $T > \theta_D$.[31] The theoretical disorder scattering parameter was obtained using both Eqs. (9) and (10) in the main text. For the strain field fluctuation, ε is directly estimated by:[32]

$$\varepsilon = \frac{2}{9}\left[\left(4+6.4\gamma\right)\frac{1+\upsilon_p}{1-\upsilon_p}\right]^2, \tag{S8}$$

where γ is the Grüneisen parameter and υ_p is the Poison ratio:

$$\upsilon_p = \frac{1-2\left(\upsilon_t/\upsilon_l\right)^2}{2-2\left(\upsilon_t/\upsilon_l\right)^2} \text{ and } \gamma = \frac{3}{2}\left(\frac{1+\upsilon_p}{2-3\upsilon_p}\right), \tag{S9}$$

with υ_t and υ_l as transverse and longitudinal sound velocities (1900 m s^{-1} and 3290 m s^{-1},[17] respectively).

The disorder scattering parameter of the experimental data (including both effects from dopants and vacancies) was obtained using the Klemens model.[33] This model predicts the ratio of the lattice thermal conductivities of a material containing defects (κ_L^{doped}) to that of the parent material (κ_L^{pure}) and can be written as:

$$\frac{\tan^{-1} u}{u} = \frac{\kappa_{\mathrm{L}}^{\mathrm{doped}}}{\kappa_{\mathrm{L}}^{\mathrm{pure}}} \quad \text{and} \quad u^2 = \frac{\pi^2 \theta_D \Omega \kappa_{\mathrm{L}}^{\mathrm{pure}} \Gamma_{\mathrm{exp}}}{h v_a}, \tag{S10}$$

where u is the disorder scaling parameter, θ_{D} is the Debye temperature, Ω is the average atomic volume, v_a is the average sound velocity and Γ is the disorder scattering parameter, respectively.

$$\upsilon_a = \left[\frac{1}{3} \left(\frac{1}{\upsilon_l^3} + \frac{2}{\upsilon_t^3} \right) \right]^{-1/3}. \tag{S11}$$

The mass-difference scattering for vacancy is given by similar to Eq. (9) in the main text expression:

$$\Phi = \frac{\sum_{i=1}^{n} c_i \left(\frac{\overline{M}_i}{\overline{\overline{M}}} \right)^2 f_i^1 f_i^{vac} \left(\frac{M_i^1 - M_{vac}}{\overline{M}_i} \right)^2}{\sum_{i=1}^{n} c_i} \quad \text{and} \quad \overline{M}_i = \sum_k \left(1 - f_i^{vac}\right) M_i^k, \tag{S12}$$

Here $f_i^1 f_i^{vac} \left(M_i^1 - M_{vac}\right)^2 = \left(1 - f_i^{vac}\right)\left(M_i^1 - \left(1 - f_i^{vac}\right) M_i^1\right)^2 + f_i^{vac} \left(0 - \left(1 - f_i^{vac}\right) M_i^1\right)^2$. However, by virial-theorem treatment for broken bonds, the above expression should be adjusted by tripling the mass difference on vacancy sites to provide more accurate calculations as proposed by R. Gurunathan *et al.*:[34]

$$f_i^1 f_i^{vac} \left(M_i^1 - M_{vac}\right)^2 = \left(1 - f_i^{vac}\right)\left(M_i^1 - \left(1 - f_i^{vac}\right) M_i^1\right)^2 + f_i^{vac} \left(-M_i^1 - 2\overline{\overline{M}}\right)^2 \tag{S13}$$

Calculated fitting coefficients are displayed in Table S2. As expected, the point defect scattering contributes to the thermal conductivity reduction by the mass and strain fluctuations. The relaxation constant A increases with the doping level along with the disorder scattering parameter. It should be noted that for the BiCuSeO† sample the grain size, L, was assumed to be ~1000 nm, while for the samples prepared using ball milling the average grain size was assumed to be 400 nm.

Table S2. Calculated temperature and frequency independent fitting parameters based on Debye–Callaway model, calculated and experimental thermal conductivity for $Bi_{1-x}R_xCuSeO$ (R = La or Pr, x = 0 – 0.08) compounds at room temperature

Compound	$(\Gamma + \Phi)_{calc}$ ($\times 10^{-2}$)	Γ_{exp} ($\times 10^{-2}$)	A (10^{-41} s^3)	B (10^{-15} s)	$\kappa_{\mathrm{lat}}^{\mathrm{calc}}$ (W m^{-1} K^{-1})	$\kappa_{\mathrm{lat}}^{\mathrm{exp}}$ (W m^{-1} K^{-1})
BiCuSeO†	–	–	0	6.31	1.24	1.30 ± 0.09
BiCuSeO	2.36	2.58	0.72	5.37	1.11	1.14 ± 0.09
$Bi_{0.98}La_{0.02}CuSeO$	3.19	6.42	1.30	5.35	0.97	0.99 ± 0.08
$Bi_{0.96}La_{0.04}CuSeO$	4.00	7.88	1.79	4.83	0.95	0.95 ± 0.08
$Bi_{0.94}La_{0.06}CuSeO$	4.82	8.29	2.53	4.17	0.93	0.94 ± 0.08
$Bi_{0.94}La_{0.08}CuSeO$	5.62	9.08	4.39	2.96	0.90	0.92 ± 0.08
$Bi_{0.98}Pr_{0.02}CuSeO$	3.14	3.91	1.78	6.57	1.11	1.08 ± 0.08
$Bi_{0.96}Pr_{0.04}CuSeO$	3.91	7.54	2.91	3.64	0.96	0.96 ± 0.08
$Bi_{0.94}Pr_{0.06}CuSeO$	4.68	5.84	0.73	5.95	1.05	1.01 ± 0.08
$Bi_{0.92}Pr_{0.08}CuSeO$	5.45	6.80	3.11	3.52	0.95	0.98 ± 0.08

References

(1) Ren, G.-K.; Wang, S.-Y.; Zhu, Y.-C.; Ventura, K. J.; Tan, X.; Xu, W.; Lin, Y.-H.; Yang, J.; Nan, C.-W. Enhancing Thermoelectric Performance in Hierarchically Structured BiCuSeO by Increasing Bond Covalency and Weakening Carrier–Phonon Coupling. *Energy Environ. Sci.* **2017**, *10* (7), 1590–1599. https://doi.org/10.1039/C7EE00464H.

(2) Barreteau, C.; Bérardan, D.; Amzallag, E.; Zhao, L.; Dragoe, N. Structural and Electronic Transport Properties in Sr-Doped BiCuSeO. *Chem. Mater.* **2012**, *24* (16), 3168–3178. https://doi.org/10.1021/cm301492z.

(3) Lazarev, V. B.; Izotov, A. D.; Gavrichev, K. S.; Shebershneva, O. V. Fractal Model of Heat Capacity for Substances with Diamond-like Structures. *Thermochim. Acta* **1995**, *269–270*, 109–116. https://doi.org/10.1016/0040-6031(95)02529-4.

(4) Barreteau, C.; Pan, L.; Amzallag, E.; Zhao, L. D.; Bérardan, D.; Dragoe, N. Layered Oxychalcogenide in the Bi–Cu–O–Se System as Good Thermoelectric Materials. *Semicond. Sci. Technol.* **2014**, *29* (6), 064001. https://doi.org/10.1088/0268-1242/29/6/064001.

(5) Pan, L.; Bérardan, D.; Zhao, L.; Barreteau, C.; Dragoe, N. Influence of Pb Doping on the Electrical Transport Properties of BiCuSeO. *Appl. Phys. Lett.* **2013**, *102* (2), 023902. https://doi.org/10.1063/1.4775593.

(6) Pei, Y.-L.; Wu, H.; Wu, D.; Zheng, F.; He, J. High Thermoelectric Performance Realized in a BiCuSeO System by Improving Carrier Mobility through 3D Modulation Doping. *J. Am. Chem. Soc.* **2014**, *136* (39), 13902–13908. https://doi.org/10.1021/ja507945h.

(7) Liu, Y.; Ding, J.; Xu, B.; Lan, J.; Zheng, Y.; Zhan, B.; Zhang, B.; Lin, Y.; Nan, C. Enhanced Thermoelectric Performance of La-Doped BiCuSeO by Tuning Band Structure. *Appl. Phys. Lett.* **2015**, *106* (23), 233903. https://doi.org/10.1063/1.4922492.

(8) Li, J.; Sui, J.; Pei, Y.; Barreteau, C.; Berardan, D.; Dragoe, N.; Cai, W.; He, J.; Zhao, L.-D. A High Thermoelectric Figure of Merit $ZT > 1$ in Ba Heavily Doped BiCuSeO Oxyselenides. *Energy Environ. Sci.* **2012**, *5* (9), 8543. https://doi.org/10.1039/c2ee22622g.

(9) Novitskii, A. P.; Khovaylo, V. V.; Mori, T. Recent Developments and Progress on BiCuSeO Based Thermoelectric Materials. *Nanobiotechnology Reports* **2021**, *16* (3), 294–307. https://doi.org/10.1134/S2635167621030150.

(10) Hiramatsu, H.; Yanagi, H.; Kamiya, T.; Ueda, K. Crystal Structures, Optoelectronic Properties, and Electronic Structures of Layered Oxychalcogenides *M*CuO*Ch* (*M* = Bi, La; *Ch* = S, Se, Te): Effects of Electronic Configurations of M^{3+} Ions. *Chem. Mater.* **2008**, *20* (10), 326–334. https://doi.org/10.1021/cm702303r.

(11) M Ganose, A.; J Jackson, A.; O Scanlon, D. Sumo: Command-Line Tools for Plotting and Analysis of Periodic Ab Initio Calculations. *J. Open Source Softw.* **2018**, *3* (28), 717. https://doi.org/10.21105/joss.00717.

(12) Kang, H.; Li, J.; Liu, Y.; Guo, E.; Chen, Z.; Liu, D.; Fan, G.; Zhang, Y.; Jiang, X.; Wang, T. Optimizing the Thermoelectric Transport Properties of BiCuSeO *via* Doping with the Rare-Earth Variable-Valence Element Yb. *J. Mater. Chem. C* **2018**, *6* (31), 8479–8487. https://doi.org/10.1039/C8TC02700E.

(13) Li, F.; Li, J.-F.; Zhao, L.-D.; Xiang, K.; Liu, Y.; Zhang, B.-P.; Lin, Y.-H.; Nan, C.-W.; Zhu, H.-M. Polycrystalline BiCuSeO Oxide as a Potential Thermoelectric Material. *Energy Environ. Sci.* **2012**, *5* (5), 7188. https://doi.org/10.1039/c2ee21274a.

(14) Zhao, L. D.; Berardan, D.; Pei, Y. L.; Byl, C.; Pinsard-Gaudart, L.; Dragoe, N. $Bi_{1-x}Sr_xCuSeO$ Oxyselenides as Promising Thermoelectric Materials. *Appl. Phys. Lett.* **2010**, *97* (9), 092118. https://doi.org/10.1063/1.3485050.

(15) Burkov, A. T.; Heinrich, A.; Konstantinov, P. P.; Nakama, T.; Yagasaki, K. Experimental Set-up for Thermopower and Resistivity Measurements at 100 – 1300 K. *Meas. Sci. Technol.* **2001**, *12*, 264–272. https://doi.org/10.1088/0957-

0233/12/3/304.

(16) Sui, J.; Li, J.; He, J.; Pei, Y.-L.; Berardan, D.; Wu, H.; Dragoe, N.; Cai, W.; Zhao, L.-D. Texturation Boosts the Thermoelectric Performance of BiCuSeO Oxyselenides. *Energy Environ. Sci.* **2013**, *6* (10), 2916. https://doi.org/10.1039/c3ee41859f.

(17) Zhao, L.-D.; He, J.; Berardan, D.; Lin, Y.; Li, J.-F.; Nan, C.; Dragoe, N. BiCuSeO Oxyselenides: New Promising Thermoelectric Materials. *Energy Environ. Sci.* **2014**, *7*, 2900–2924. https://doi.org/10.1039/c4ee00997e.

(18) Feng, B.; Li, G.; Pan, Z.; Hu, X.; Liu, P.; He, Z.; Li, Y.; Fan, X. Enhanced Thermoelectric Properties in BiCuSeO Ceramics by Pb/Ni Dual Doping and 3D Modulation Doping. *J. Solid State Chem.* **2019**, *271*, 1–7. https://doi.org/10.1016/j.jssc.2018.12.001.

(19) Kireev, P. S. *Semiconductor Physics*, 2nd ed.; Mir: Moscow, 1978.

(20) Fistul', V. I. *Heavily Doped Semiconductors*; Springer New York: Boston, MA, 1995. https://doi.org/10.1007/978-1-4684-8821-0.

(21) Bonch-Bruevich, V. L.; Kalashnikov, S. G. *Semiconductor Physics*; Nauka: Moscow, 1977.

(22) *Materials Aspect of Thermoelectricity*; Uher, C., Ed.; CRC Press: Boca Raton, 2017.

(23) Li, J.; Sui, J.; Pei, Y.; Meng, X.; Berardan, D.; Dragoe, N.; Cai, W.; Zhao, L.-D. The Roles of Na Doping in BiCuSeO Oxyselenides as a Thermoelectric Material. *J. Mater. Chem. A* **2014**, *2* (14), 4903–4906. https://doi.org/10.1039/c3ta14532h.

(24) Pei, Y.-L.; He, J.; Li, J.-F.; Li, F.; Liu, Q.; Pan, W.; Barreteau, C.; Berardan, D.; Dragoe, N.; Zhao, L.-D. High Thermoelectric Performance of Oxyselenides: Intrinsically Low Thermal Conductivity of Ca-Doped BiCuSeO. *NPG Asia Mater.* **2013**, *5* (5), e47. https://doi.org/10.1038/am.2013.15.

(25) Sun Lee, D.; An, T.-H.; Jeong, M.; Choi, H.-S.; Soo Lim, Y.; Seo, W.-S.; Park, C.-H.; Park, C.; Park, H.-H. Density of State Effective Mass and Related Charge Transport Properties in K-Doped BiCuOSe. *Appl. Phys. Lett.* **2013**, *103* (23), 232110. https://doi.org/10.1063/1.4837475.

(26) Novitskii, A.; Serhiienko, I.; Novikov, S.; Kuskov, K.; Pankratova, D.; Sviridova, T.; Voronin, A.; Bogach, A.; Skryleva, E.; Parkhomenko, Y.; Burkov, A.; Mori, T.; Khovaylo, V. Thermoelectric Properties of Sm-Doped BiCuSeO Oxyselenides Fabricated by Two-Step Reactive Sintering. *J. Alloys Compd.* **2022**, *912*, 165208. https://doi.org/10.1016/j.jallcom.2022.165208.

(27) Novitskii, A.; Guélou, G.; Moskovskikh, D.; Voronin, A.; Zakharova, E.; Shvanskaya, L.; Bogach, A.; Vasiliev, A.; Khovaylo, V.; Mori, T. Reactive Spark Plasma Sintering and Thermoelectric Properties of Nd-Substituted BiCuSeO Oxyselenides. *J. Alloys Compd.* **2019**, *785* (15), 96–104. https://doi.org/10.1016/j.jallcom.2019.01.183.

(28) Feng, B.; Jiang, X.; Pan, Z.; Hu, L.; Hu, X.; Liu, P.; Ren, Y.; Li, G.; Li, Y.; Fan, X. Preparation, Structure, and Enhanced Thermoelectric Properties of Sm-Doped BiCuSeO Oxyselenide. *Mater. Des.* **2020**, *185*, 108263. https://doi.org/10.1016/j.matdes.2019.108263.

(29) Kang, H.; Zhang, X.; Wang, Y.; Li, J.; Liu, D.; Chen, Z.; Guo, E.; Jiang, X.; Wang, T. Enhanced Thermoelectric Performance of Variable-Valence Element Sm-Doped BiCuSeO Oxyselenides. *Mater. Res. Bull.* **2020**, *126*, 110841. https://doi.org/10.1016/j.materresbull.2020.110841.

(30) Feng, B.; Li, G.; Pan, Z.; Hu, X.; Liu, P.; Li, Y.; He, Z.; Fan, X. Enhanced Thermoelectric Performances in BiCuSeO Oxyselenides *via* Er and 3D Modulation Doping. *Ceram. Int.* **2019**, *45* (4), 4493–4498. https://doi.org/10.1016/j.ceramint.2018.11.130.

(31) Slack, G. A.; Galginaitis, S. Thermal Conductivity and Phonon Scattering by Magnetic Impurities in CdTe. *Phys. Rev.*

1964, *133* (1A), A253–A268. https://doi.org/10.1103/PhysRev.133.A253.

(32) Abeles, B. Lattice Thermal Conductivity of Disordered Semiconductor Alloys at High Temperatures. *Phys. Rev.* **1963**, *131* (5), 1906–1911. https://doi.org/10.1103/PhysRev.131.1906.

(33) Klemens, P. G. Thermal Resistance Due to Point Defects at High Temperatures. *Phys. Rev.* **1960**, *119* (2), 507–509. https://doi.org/10.1103/PhysRev.119.507.

(34) Gurunathan, R.; Hanus, R.; Dylla, M.; Katre, A.; Snyder, G. J. Analytical Models of Phonon–Point-Defect Scattering. *Phys. Rev. Appl.* **2020**, *13* (3), 034011. https://doi.org/10.1103/PhysRevApplied.13.034011.